Journal of Photochemistry and Photobiology A: Chemistry 199 (2008) 156–164

Contents lists available at ScienceDirect

Journal of Photochemistry and Photobiology A: Chemistry

journal homepage: www.elsevier.com/locate/jphotochem

UV laser photolytic solution deposition of a-Fe/polyoxocarbosilane/carbon nanocomposite and evolution to α-Fe_2O_3/polyoxocarbosilane/carbon nanocomposite

J. Pola[a,*], M. Maryško[b], V. Vorlíček[b], S. Bakardjieva[c], J. Šubrt[c], Z. Bastl[d], A. Ouchi[e,**]

[a] Laboratory of Laser Chemistry, Institute of Chemical Process Fundamentals, Rozvojova Street 135, ASCR, 16502 Prague, Czech Republic
[b] Institute of Physics, ASCR, 18221 Prague 8, Czech Republic
[c] Institute of Inorganic Chemistry, ASCR, 25068 Řež, Czech Republic
[d] J. Heyrovský Institute of Physical Chemistry, ASCR, 18223 Prague 8, Czech Republic
[e] National Institute of Advanced Industrial Science and Technology, AIST, Tsukuba, Ibaraki 305-8565, Japan

ARTICLE INFO

Article history:
Received 14 December 2007
Received in revised form 7 May 2008
Accepted 13 May 2008
Available online 20 May 2008

Keywords:
Laser photolysis
Fe(II) acetylacetonate
Laser solution-deposition
a-Iron/polyoxocarbosilane/carbon nanocomposite
Laser backside silica etching
α-Iron oxide/polyoxocarbosilane/carbon nanocomposite
Superantiferromagnetism

ABSTRACT

KrF laser-induced photolysis of Fe(II) acetylacetonate in 2-propanol leads to (i) formation of nanosized iron and (ii) etching of the silica reactor by carbonaceous photolytic products, yielding amorphous polyoxocarbosilane. These reactions allow chemical solution deposition of Fe/polyoxocarbosilane/carbon nanocomposite possessing rare amorphous Fe phase. The material in ambient air undergoes slow oxidative passivation of the Fe constituent forming a discontinuous a-Fe_2O_3 shell and when heated it transforms to nanosized crystalline α-Fe_2O_3/polyoxocarbosilane/carbon nanocomposite. Its magnetic moment is a superposition of ferromagnetic contribution from large particles and superantiferromagnetic contribution from the thin passivating shell.

1. Introduction

Magnetic zero-valent iron and iron oxide nanoparticles and their nanocomposites with the nanoparticles separated in a non-magnetic medium have become of great interest due to their promising applications as magnetic gels [1], in targeted magnetic resonance imaging (e.g. [2]), separation of bioactive substances (e.g. [3–5]) and also as sensors [6,7], catalysts and sorbents for environmental remediation [8,9].

Iron nanoparticles were obtained by thermal decomposition (e.g. [10–12]), chemical vapour deposition [13] and vapour phase condensation [14] processes from iron pentacarbonyl, by chemical reduction of iron salts (e.g. [15,16]) and by exploding wire technique [17]. The iron oxides nanoparticles were prepared by chemical reactions of Fe ions in aqueous solution (e.g. [18–21]) and high temperature reactions of Fe complexes [22–24] and were stabilized in non-polar liquid phase with surfactants (e.g. [25–27]).

The nanocomposites of iron particles are less common that their iron oxide counterparts. The Fe/polymer nanocomposites were obtained by sonolysis of iron pentacarbonyl in anisol in the presence of poly(dimethylphenyleneoxide) [28], heating of iron pentacarbonyl and styrene solution [29] and hydrolytic polycondensation of tetraethoxysilane on the surface of Fe particles [30]. The more common Fe/carbon nanocomposites were prepared by e.g. heating an aromatic oil and ferrocene [31], in an arc discharge in ethanol vapour [32], by annealing iron and diamond nanoparticles in vacuum [33] and IR laser co-pyrolysis of ethylene and iron pentacarbonyl (e.g. [34]).

Much recent attention was also given to iron oxide nanoparticles in dielectric phase; these composites offer possibility to stabilize magnetic nanoparticles in dielectric media and tailor their properties through control of variables of their synthetic procedures. The iron oxide/dielectric phase nanocomposite were

* Corresponding author. Tel.: +420 2 20390308; fax: +420 2 20920661.
** Corresponding author. Tel.: +81 29 861 4550; fax: +81 29 861 4421.
E-mail addresses: pola@icpf.cas.cz (J. Pola), ouchi.akihiko@aist.go.jp (A. Ouchi).

1010-6030/$ – see front matter © 2008 Elsevier B.V. All rights reserved.
doi:10.1016/j.jphotochem.2008.05.014

produced by incorporation of Fe_2O_3 nanoparticles into organic polymers [5,35–41], mesoporous silica [42,43], glass [44,45] and silicon oxide [6,46–53]. The Fe_2O_3/SiO_2 nanocomposites are available from iron compounds and silicon alkoxide through different sol–gel techniques. Their size, phase of magnetic constituents and the proportion of the magnetic and non-magnetic phase is affected [49,51–54] by conditions of the sol–gel procedure and subsequent thermal processing.

We have previously reported on the feasibility of UV laser-induced solution photolysis of organometallic compounds for deposition of nanostructured germanium films [55], Te and Te/C nanoparticles [56] and Fe-based nanoparticles [57]. We have also shown that UV laser-induced solution photolysis of Cu(II) acetylacetonate allows chemical liquid deposition of discontinuous and continuous copper films [58] and formation of Cu/polymer colloids and nanocomposites [59]. These photolytic procedures are clean processes not requiring additional chemical reagents and a special work-up of the resulting reaction products.

It was of our further interest to examine whether UV laser-induced solution photolysis of Fe(II) acetylacetonate is feasible for formation of Fe-based nanofeatures. Here we show that this reaction represents a clean, one-step synthesis of amorphous iron/polyoxocarbosilane/carbon nanocomposites. We also report on the stability and physical properties of this material.

2. Experimental

Samples of Fe(II) acetylacetonate (Aldrich, 30 ml of 2×10^{-3} M solutions in 2-propanol (Cica-reagent for spectroscopy)) were placed in a quartz tube (3 cm in diameter, 10 cm long) equipped with a valve for connection to a vacuum line. The orange solutions (50 ml) were de-aerated by using vacuum (three freeze–thaw cycles), bubbled with Ar for more than half an hour and irradiated under Ar with an LPX-200 (Lambda Physik) laser. The KrF laser radiation at 248 nm at a repetition frequency of 10 Hz delivering energy of 650 mJ/pulse (measured by a Gentec ED-500 joulmeter) was employed. The solutions were stirred by a magnetic bar and the laser pulses were mildly focused to incident area of 1.2 cm^2 to get incident fluence of 540 mJ/cm^2.

The photolytic progress was monitored on aliquots (0.3 ml) withdrawn from the irradiated solution and diluted with 3 ml of 2-propanol by UV–vis spectrometry (a Shimadzu UV-2450 UV–VIS spectrometer) in the 4 ml quartz cells.

After the photolysis, the solutions were allowed to stay overnight and black particles precipitated during this period were centrifuged from the solutions and washed with hexane. The centrifuged solutions were analyzed on a Shimadzu QP5050 gas chromatograph–mass spectrometer (60 m long capillary column with Neutrabond-1 as a stationary phase, programmed temperature 30–200 °C) and detected photolytic products were identified by using the NIST library.

The sediment was analyzed by UV spectroscopy (an UV 1601 Shimadzu spectrophotometer), FTIR spectroscopy (a Nicolet Impact spectrometer), by Raman spectroscopy, X-ray photoelectron spectroscopy and by electron microscopy.

The Raman spectra were acquired on a Renishaw (a Ramascope model 1000) Raman microscope coupled with a CCD detector and excitation radiations of He–Ne (633 nm). The excitation beam was defocused to obtain lower energy density and diminish sample heating.

The X-ray photoelectron spectra were measured with a Gammadata Scienta ESCA 310 electron spectrometer using monochromatized Al Kα ($h\alpha$ = 1486.6 eV) radiation for electron excitation. The high-resolution spectra of Fe 2p, Si 2p, C 1s and O 1s photoelectrons were measured for an as-received sample. Quantification of the element concentration ratios was accomplished by correcting the photoelectron peak intensities for their cross-sections [60] and accounting for the dependence of the inelastic mean free path of photoelectrons on their kinetic energy [61]. Curve fitting of overlapping lines was carried out using the lines of a Gaussian–Lorentzian shape. Core level binding energies were determined with an accuracy ±0.2 eV.

The SEM images were acquired using a Philips XL30 CP scanning electron microscope. The TEM analysis (particle size and phase analysis) was carried out on a Philips 201 transmission electron microscope. HRTEM micrographs were obtained using a JEOL JEM 3010 operating at 300 kV (LaB6 cathode) and equipped with EDS detector (INCA/Oxford). Nickel grid coated with a holey carbon support film was used. Sediments were dispersed in ethanol and suspension was treated in ultrasonic bath for 10 min.

The magnetic measurements were carried out in the temperature region 5–350 K using a SQUID magnetometer MPMS-5S (Quantum Design).

3. Results and discussion

3.1. Laser photolysis

Iron(II) acetylacetonate shows UV absorption bands at 207, 237, 272, 348 and 428 nm (Fig. 1a) and allows an efficient absorption of the KrF laser radiation (248 nm) in π–π* transition within the ligand and/or charge-transfer transition of the ligand-to-metal type bands [62].

The laser irradiation of the orange solution of Fe(II) acetylacetonate in 2-propanol leads to the formation of tiny bubbles behind the irradiated quartz wall and development of deep brown colour of the solution. The spectral changes do not indicate any new bands (Fig. 1) but only an initial growth and a subsequent depletion of the 272 and 237 nm bands, which is consistent with the formation and decay of a transient species of spectral pattern similar to that of Iron(II) acetylacetonate.

GC/MS analysis of the irradiated solution indicated formation of carbon monoxide, acetone, 1-methylethyl acetate and 1-methyl-3-oxo-but-1-enyl acetate. These compounds are in line with (i) a decomposition of the ligand and/or transiently formed acetylacetone and (ii) reactions of acetylacetone photofragments with 2-propanol [59]. Low quantities of the detected products are in keeping [59] with reactions leading to higher molecular substances. The brown solution of the irradiated Fe(II) acetylacetonate staying

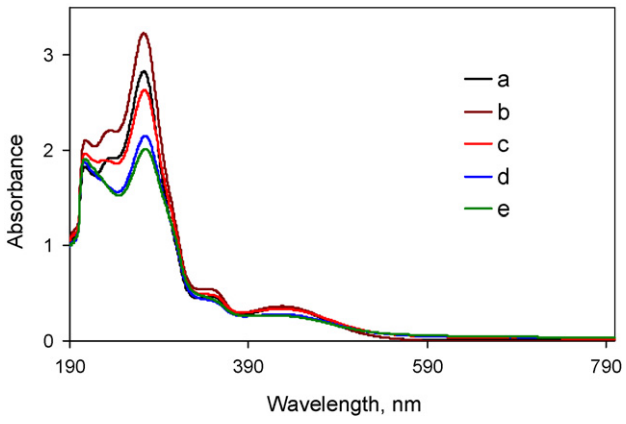

Fig. 1. UV/vis absorption spectra of the diluted solution of Fe(II) acetylacetonate (2×10^{-3} M solutions in 2-propanol) before (a) and after 60 (b), 120 (c), 180 min (d) and 240 min (e) irradiation.

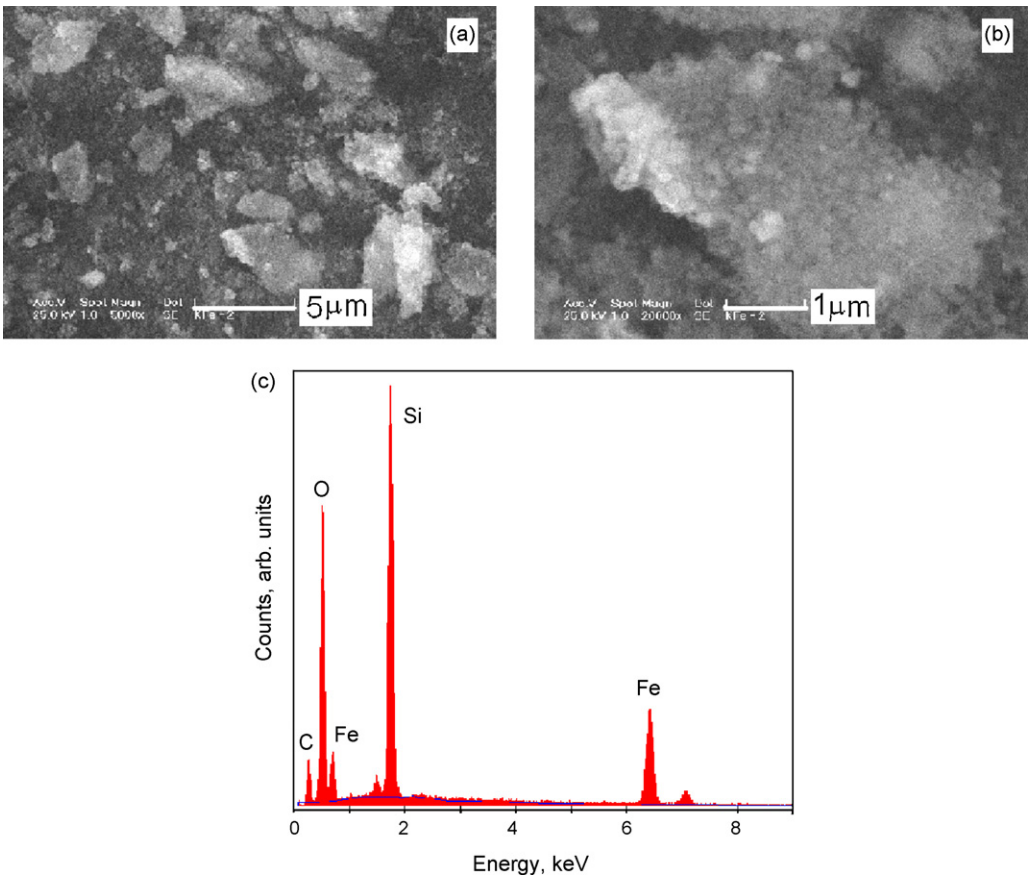

Fig. 2. SEM image (a and b) and EDX-SEM analysis (c) of the sediment.

overnight yields a black sediment and does not change the UV/vis absorption spectral pattern.

3.2. Composition and spectral properties of the sediment

The SEM and EDX-SEM analysis (Fig. 2) reveals that the sediments is formed by 1–5 μm-sized bodies and composed of C, O, Fe and O elements. The determined stoichiometry – $Fe_{1.00}Si_{2.20}C_{5.36}O_{7.30}$ – indicates that Fe is present in lower concentration than the other elements.

The electron diffraction patterns and TEM and HRTEM images (Fig. 3) are consistent with an amorphous phase and aggregated, ca. 10 nm-sized bodies. The images also show some 50–200 nm-sized dark (full) and lighter (empty) spherical bodies. Selective area EDX analysis reveals that the darker bodies are significantly richer in Fe. Thus, e.g. the Fe/Si/O atomic% ratio for the darker and lighter areas is respectively 1/0.15/0.11 and 1/0.53/0.47. These values also show that a-Fe phase co-exists with a material possessing equal amounts of Si and O elements.

The predominance of the amorphous Fe state has been confirmed by laborious examination of many ED patterns which indicated that crystalline Fe phase is practically absent and very marginally occurs [63] as hexagonal Fe (PDF 34-0529, Fig. 4).

The stoichiometry of superficial (several nanometer thick) layers calculated from integrated intensities of photoelectron spectra – $Fe_{1.00}Si_{10.0}C_{17.1}O_{24.6}$ – indicates that the concentration of Fe at the sediment surface is lower than in deeper layers (~0.5 μm) as derived from the EDX-SEM measurement. The spectrum of Fe 2p photoelectrons (Fig. 5) shows only one chemical state and the measured binding energy of $Fe2p_{3/2}$ electrons (711.4 eV) is compatible with Fe^{3+} in ferric oxide [64]. The observed pronounced increase of background towards higher binding energies in this spectrum (Fig. 5) indicates that iron oxide is covered by a layer responsible for inelastic scattering of Fe 2p electrons. The spectrum of Si 2p photoelectrons peaked at 103.0 eV is consistent with SiO_2 [64] and/or (Si/C/O) structures with low content of C [65]. The spectrum of C 1s electrons is dominated by a major contribution at 284.6 eV assigned to C–C bonds; a minor component at 287.6 eV relates to carbon in C=O bonds. The O 1s spectrum is a superposition of a less intense component located at 530.0 eV (Fe_2O_3) and that centered at 532.7 eV and related to SiO_2 and (Si/C/O) structures.

The FTIR absorption spectrum of the sediment (Fig. 6) shows typical pattern of polyoxocarbosilanes [66] dominated by a very strong absorption band at 1050 cm^{-1} (ν^{as}(SiOSi)). Other less distinctive features at 810, 900, 1270 and 1600 cm^{-1} are respectively assignable [67] to ν(Si–C), ν(SiOSi(OH)), $\delta(SiCH_x)$ and ν(C=C) vibrational modes. The weak absorption bands between 540 and 470 cm^{-1} are tentatively assigned to symmetrical stretching modes of siloxane units. The spectrum shows neither a week δ(OSiO) band at 510 cm^{-1} related [68] to SiO_2, nor any evidence on Fe_2O_3 at 550 cm^{-1}. The latter is in agreement with the above XPS and electron microscopy measurements that are compatible with very minor occurrence of this oxide in topmost layers of a-Fe bodies.

The UV–vis spectrum of the sediment washed with hexane and ultrasonically dispersed in 2-propanol (Fig. 7) shows an enhanced absorption between 220 and 350 nm which can be attributed to contributions of both surface plasmon of the nanosized Fe-based core [68–71] and CT bands of superficial films of iron oxide [72]. The declining continuous absorption at higher wavelength suggests some degree of conjugation of the C=C bonds.

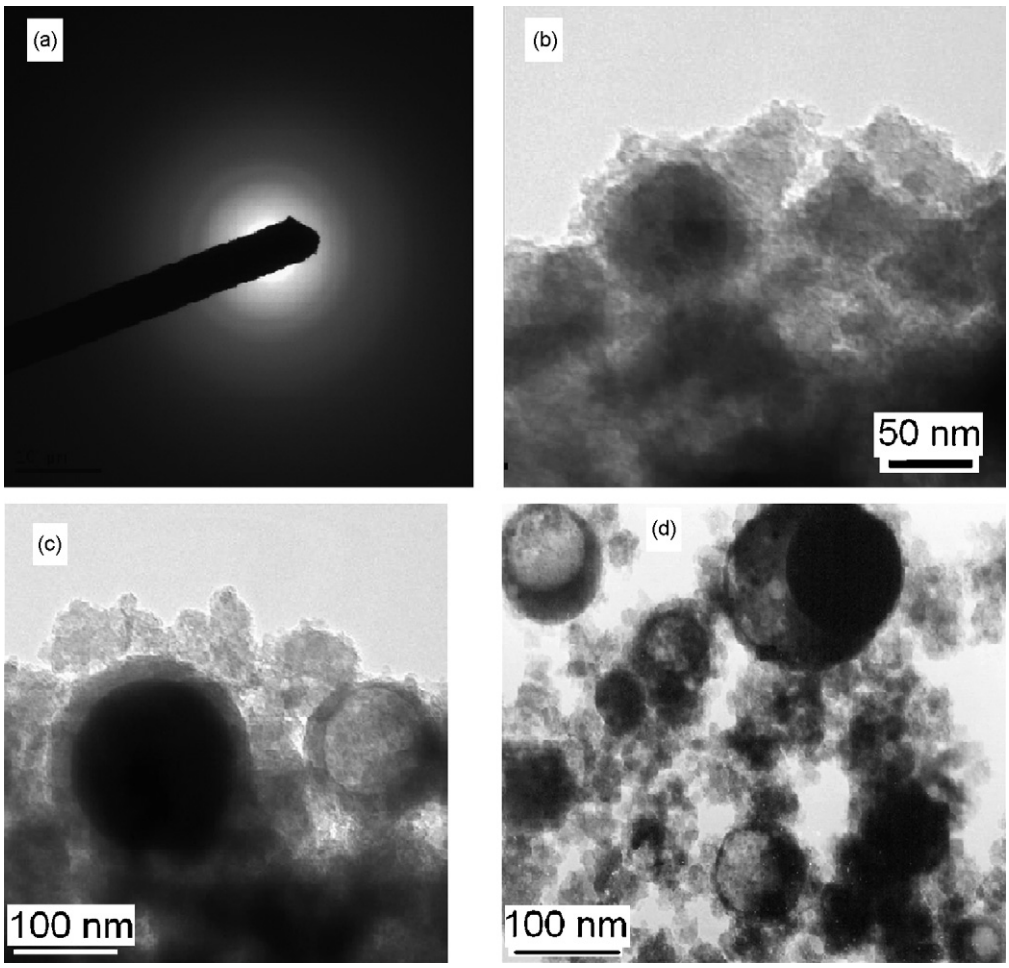

Fig. 3. Electron diffraction (a), HRTEM (b and c) and TEM (d) images of the sediment.

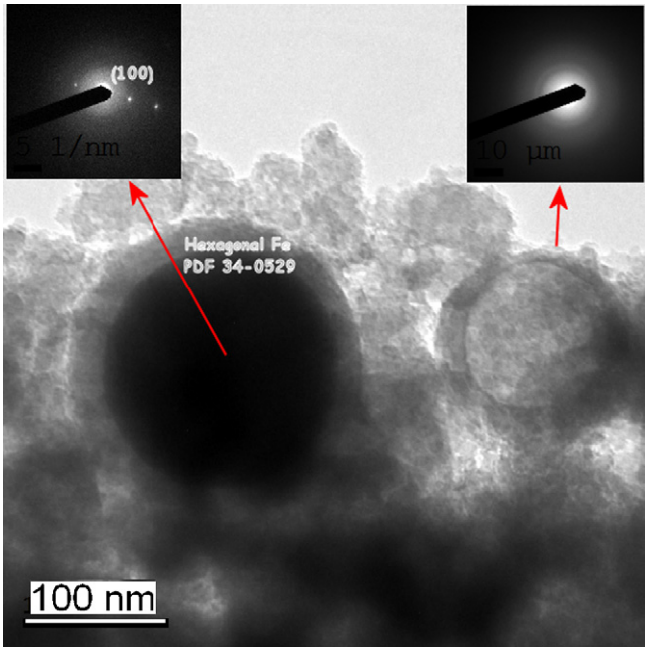

Fig. 4. Electron diffraction and TEM image confirming marginal crystalline Fe features.

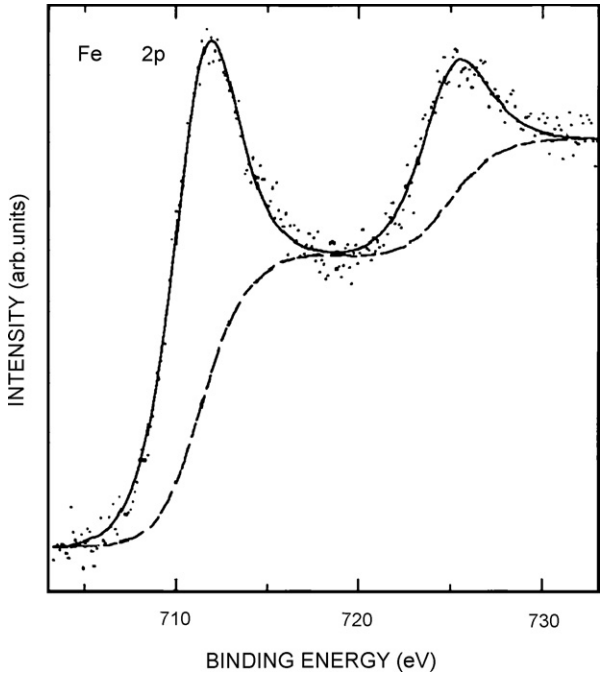

Fig. 5. Spectrum of Fe 2p photoelectrons of the sediment.

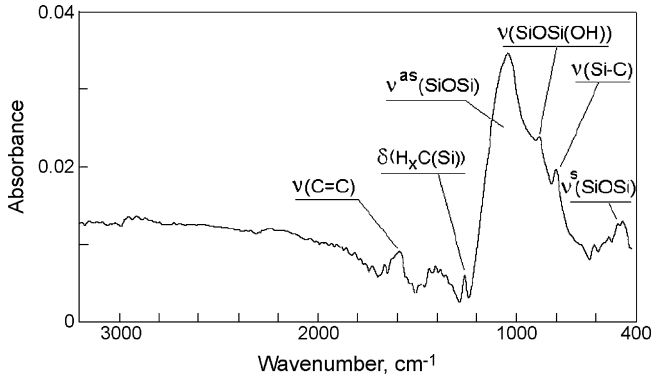

Fig. 6. FTIR spectrum of the sediment film on KBr.

3.3. Magnetic properties of the sediment

The basic information on magnetic properties of the sediment was obtained from the virgin magnetization curves $m(H)$ (corrected for the diamagnetic signal of the holder, Fig. 8) and from the temperature dependence of the coercivity (Fig. 9a) and of the remanent magnetization (Fig. 9b) which were evaluated from the hysteresis loops. The exchange bias (EB) shift $H_E \approx 28$ Oe found by comparing the field-cooled and zero-field-cooled hysteresis loops at $T = 4.5$ K points to the existence of the interfaces between the ferromagnetic (FM) and antiferromagnetic (AFM) phases.

The zero-field-cooled (ZFC) and field-cooled (FCC) susceptibilities m/H for different magnetic fields were measured during warming and cooling the sample respectively. The results are presented in Fig. 10, where we see that for $H = 5$ kOe the ZFC and FCC dependences confluence.

In the high field region, we focused our attention on the FCC dependences for $H = 20$ and 25 kOe (Fig. 11a), which may be used for evaluation of the ferromagnetic and linear susceptibility contributions to the total magnetizations (Fig. 11b and c).

In the whole temperature region, the virgin curves (Fig. 8) suggest the presence of a blocked magnetic state characterized by the FM moment and a linear susceptibility contribution. The separation of these two contributions was made under the simplified assumption that the total magnetization can be expressed as $m = m_0(T) + \chi(T)H$, where $m_0(T)$ denotes the FM magnetization and $\chi(T)$ linear susceptibility. Let us remark that even at $T = 4.5$ K the deviation from the linearity is very small and corresponds to the curvature of the Brillouin function for $S \approx 0.7$. With increasing temperature this deviation decreases and for T larger than about 60 K is too small to be detected. The measured FCC dependences for $H = 25$ and 20 kOe (Fig. 11a) were used to evaluate the $m_0(T)$ and

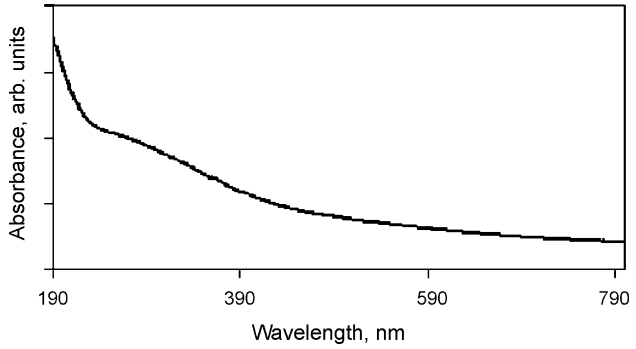

Fig. 7. UV/vis spectrum of the sediment dispersed in 2-propanol.

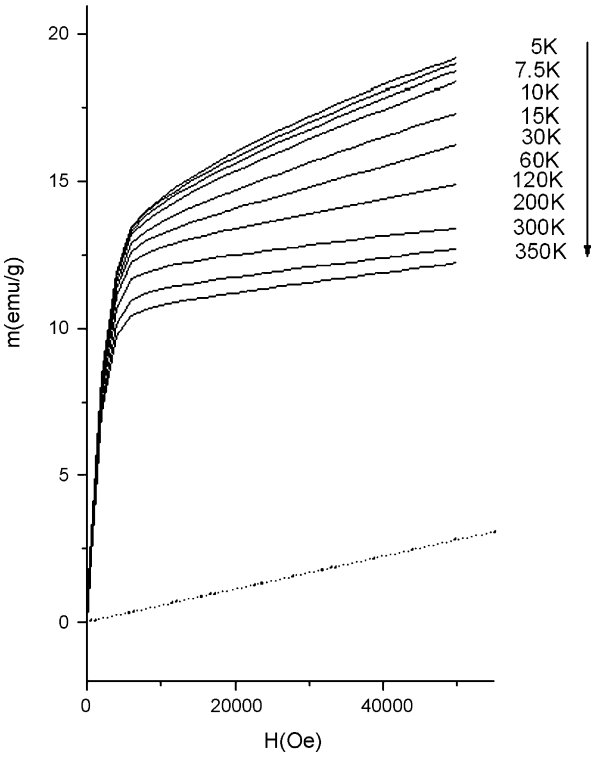

Fig. 8. Virgin magnetization curves at different temperatures, by the dotted line the correction for the diamagnetic sample holder.

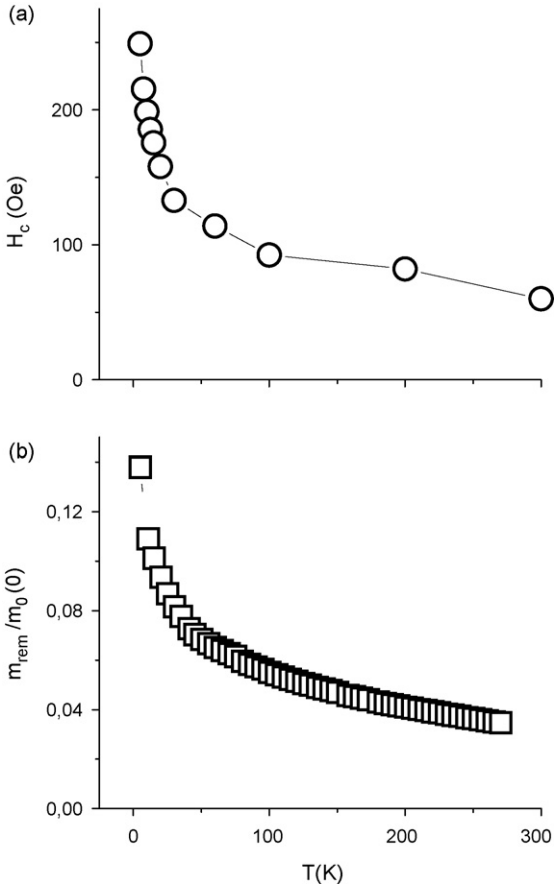

Fig. 9. Temperature dependence of the coercivity (a) and of the reduced remanent magnetization (b), $m_0(0)$ is the extrapolated FM magnetization at $T = 0$ K.

$\chi(T)$ dependences in the temperature region above 100 K, where the influence of a non-linearity can be absolutely excluded (points in the Fig. 11b and c). The dotted curve in these figures corresponds to the temperature region where the evaluation has a formal character with regard to the non-linearity mentioned above. The course of the $m_0(T)$ points to the ferromagnetic character of this contribution. The extrapolation to $T = 0$ K yields $m_0(0) = 12.38$ emu/g and at room temperature we have $m_0(300) = 10.86$ emu/g. For the weight fraction 0.186 of Fe in the sediment we can determine the room temperature magnetization 58.1 emu/g of iron (for the bulk amorphous iron we have 138.1 emu/g). The behaviour of $m_0(T)$ at high temperatures clearly suggests the blocking temperature to be higher than 400 K, which corresponds to nanoparticles having diameter larger than about 30 nm. The temperature dependence of $\chi(T)$ (Fig. 11c) resembles at first sight the Curie–Weiss law, but the presence of a large temperature independent term given by the limit of $\chi(T)$ towards higher temperatures does not correspond to the contribution of paramagnetic centers. The observed $\chi(T)$ dependence is assumed to be connected with the superantiferromagnetic behaviour of antiferromagnetic nanoparticles for which, above the blocking temperature, T_B, the susceptibility contains a temperature independent term determined by the antiferromagnetic susceptibility [73]. Namely, the bulk antiferromagnetic material exhibits the $\chi(T)$ which is nearly independent on temperature or decreases slowly with decreasing temperature. The decrease of the susceptibility with increasing temperature is therefore caused by nanodimensions of the antiferromagnetic regions and was first observed on the antiferromagnetic fine grains (2–60 nm) of NiO, Cr_2O_3 and α-Fe_2O_3 [74].

Further discussion on the results of the magnetic measurements, which takes into account the data from Section 3.2, is appropriate. The existence of weakly pronounced maxima in the ZFC susceptibilities ($T_m \approx 130$, 160, 110 K) (Fig. 10) suggests that a certain small part of the magnetic moment is produced by amorphous iron

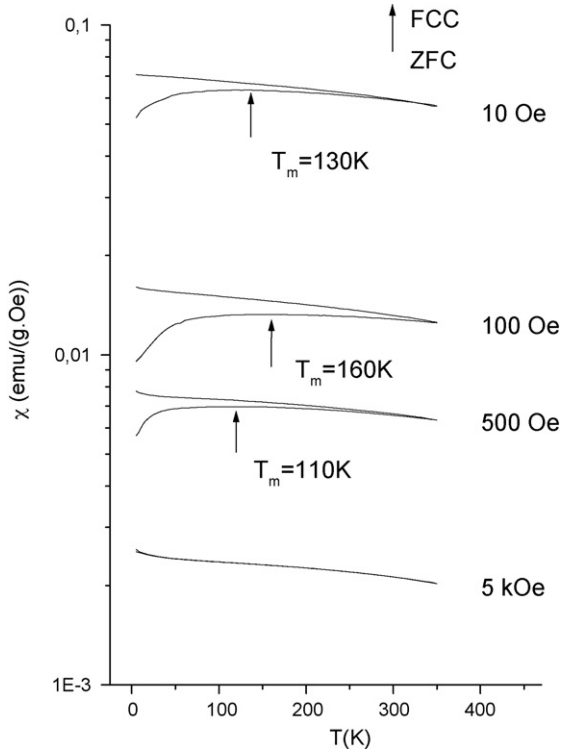

Fig. 10. ZFC and FCC susceptibilities measured for different magnetic fields, the arrows show the positions of maxima characterized by temperatures T_m.

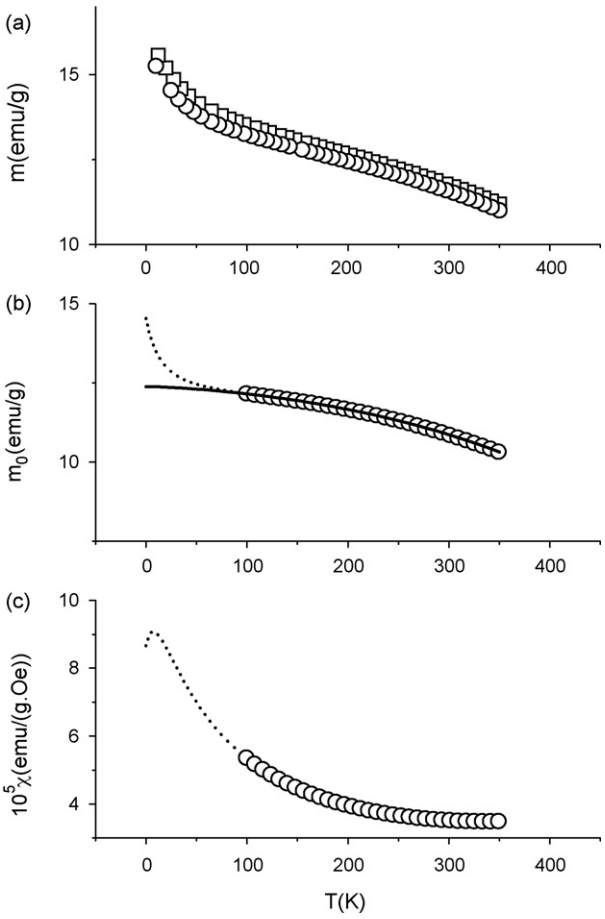

Fig. 11. FCC magnetizations for $H = 25$ and 20 kOe (a) and the evaluated temperature dependences: (b) the FM magnetization and (c) linear susceptibility.

nanoparticles with blocking temperatures near 150 K. For a typical value of the anisotropy constant 10^6 erg cm^{-3} this corresponds to the particle diameter 10 nm, which is in agreement with the TEM investigations. In this case, the relative volume of this minor FM phase with a larger coercivity, could be estimated comparing

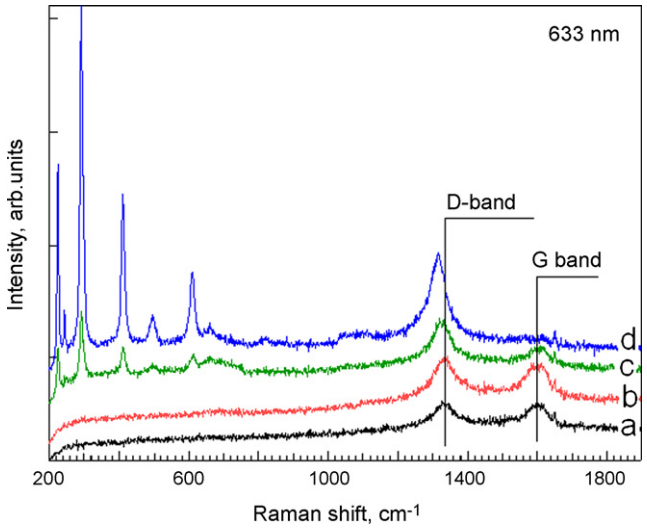

Fig. 12. Raman spectra of the sediment taken at 800 W/cm^{-2} after pre-irradiation of the sample by the exciting beam at different higher energies (a, no pre-irradiation; b, 2×10^4 W cm^{-2} for 6 min; c, 4×10^4 W cm^{-2} for 13 min; d, 8×10^4 W cm^{-2} for 3 min).

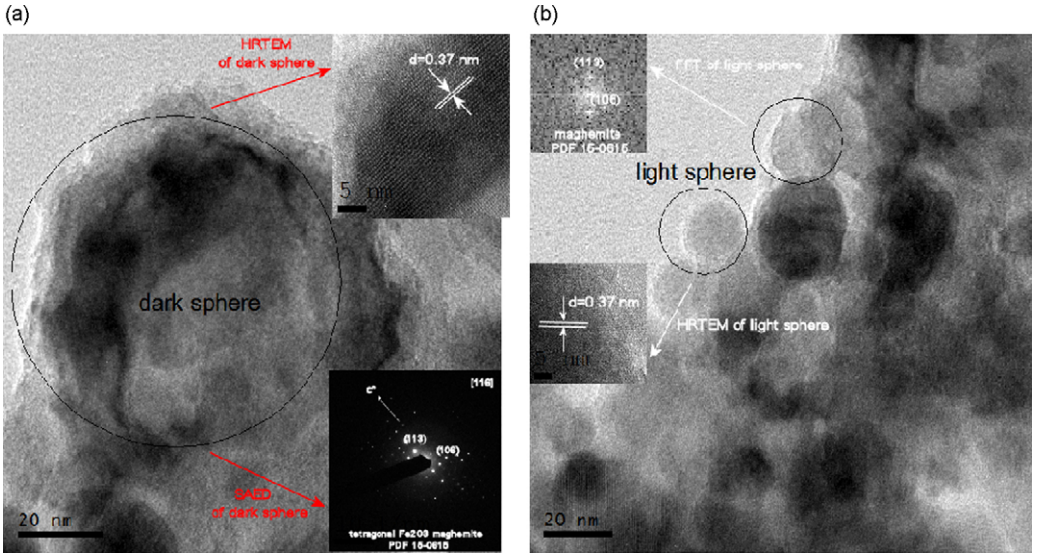

Fig. 13. HRTEM analyses of the sediment dark (a) and light (b) spheres after heating to 500 °C.

the value of the measured coercivity at 5 K with the anticipated anisotropy constant 10^6 erg cm^3. This crude estimate suggests that the FM contribution of the 10 nm iron nanoparticles represents only 1/10 of the total FM moment of the sample. The rest of the FM magnetic moment likely arises from the large amorphous/minority FCC iron particles having dimension between 50 and 200 nm. This would be in accord with the behaviour of the FM component as shown in Fig. 11b. The FCC iron can be in different paramagnetic, antiferromagnetic or ferromagnetic coordinations [75,76] and an interesting question concerns the origin of the $\chi(T)$ contribution. As mentioned above, this contribution could be connected with antiferromagnetic nanoregions. Let us recall that the presence of an antiferromagnetic phase in the sediment was proved by the measurement of a finite EB shift. The occurrence of this magnetic state is undoubtedly connected with the presence of the Fe_2O_3 oxide. It is known that α-Fe_2O_3 (hematite) represents an antiferromagnet (we ignore a small spin canting) and amorphous Fe_2O_3 has a small ferromagnetic moment [77]. Inspecting the results of the magnetic measurements [76] made on the 25 nm nanoparticles of amorphous Fe_2O_3 we see that the FM moment is accompanied by a small linear susceptibility. It is realistic to assume that for smaller nanoparticles of Fe_2O_3 this linear contribution corresponding most probably to the local antiferromagnetic arrangement will be larger. With regard to the fact that most of Fe atoms are not crystallographically coordinated (Section 3.2), we ascribe the antiferromagnetic contribution to the amorphous oxide Fe_2O_3 in the passivating shells. From the XPS diagnostics we know that iron nanoparticles are surrounded by few nanometer thick Fe_2O_3 shells. Just these shells can act as antiferromagnetic nanoparticles with the superantiferromagnetic behaviour having the blocking temperature in the low temperature, we estimate, 7–30 K region. (It can be compared with the temperature $T_m \approx 7.5$ K of the maximum on the dotted curve $\chi(T)$ in Fig. 11c.) In this situation, the $\chi(T)$ evaluated from the experiment can be explained by the superantiferromagnetic contribution of the nanosized shells.

We thus suggest that the antiferromagnetic arrangement of the magnetic moments occurs in small nanoregions formed by the amorphous Fe_2O_3 oxide. The data and the interpretation contribute to the growing field of the antiferromagnetic nanoparticles which are not as common as ferromagnetic nanoparticles.

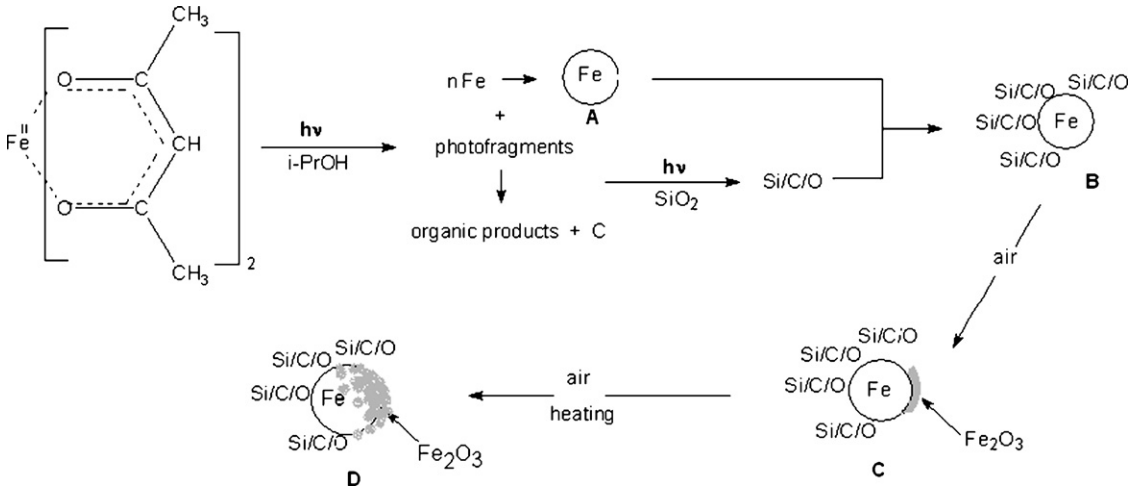

Scheme 1.

3.4. Heat-induced changes in properties of the sediment

The Raman spectra of the sediment (Fig. 12) differ depending on the period of the pre-treatment (pre-irradiation) by the exciting beam. The sample exposed to low energy excitation shows only G and D bands of disordered graphitic carbon at 1650 and 1330 cm^{-1}, respectively. With the pre-irradiated sample, these bands decline and new bands at 226, 245, 292, 411, 496, 610, 660 and 1320 cm^{-1} assignable to α-Fe_2O_3 (e.g. [78,79]) appear. Their growth is more important with higher energy of the exciting beam and the longer period of the pre-irradiation. The Raman spectra are related to the crystalline quality of the structure [80] and these changes provide evidence on heat-accelerated oxidation of iron bodies to α-Fe_2O_3 phase.

The sediment exposed to air for several days and heated in vacuum to 500 °C develops crystalline α-Fe_2O_3 phase (Fig. 13). The tetragonal lattice structure of maghemite (PDF ICDD 15-0615, [63]) was confirmed with interplanar spacing $d_{(113)}$ = 0.484 nm and $d_{(106)}$ = 0.375 nm (Fig. 13a). The SAED pattern of nanoparticles from the bulk dark sphere shows strong spot arrays which can be indexed on the basis of tetragonal Fe_2O_3 type cell with space group $P2_13$ and parameters a = 8.33 and c = 24.99. Fig. 13b (inset) is a [1 1 6] diffraction pattern of a maghemite Fe_2O_3 crystal.

We therefore assume that the amorphous Fe nanophase in the composite is fully protected by neither Fe_2O_3 passivation layer nor by the (Si/C/O) polymer/carbon and that oxidation of the Fe phase is possible only through an easy penetration of oxygen into Fe deeper layers. This process can be feasible due to intermixing of nanobodies of a-Fe phase with C and (Si/C/O) polymer and by reorganization of nanocomposite structures at high temperatures.

3.5. Probable reaction mechanism

The formation of the nanocomposite material from Fe(II) acetylacetonate can be explained in terms of (i) deep photolysis of the chelate leading to zero-valent elemental Fe and photofragments that undergo carbonization and (ii) reaction of carbonaceous excited products with silica surface leading to the formation of polyoxocarbosilane. The former path is similar to photolytic decomposition of Cu(II) acetylacetonate to elemental amorphous copper [58,59]. The latter path is analogous to the earlier reported laser-induced etching of silica by hot (excited) photoproducts (e.g. [81–83]) in the liquid phase and should involve reduction of silica by carbonaceous fragments to a highly reactive, SiO-like intermediate which undergoes further reactions to polyoxocarbosilane. Similar mechanism was suggested by us for reaction of silica with gaseous products of laser-induced decomposition of hydrocarbons, yielding nanosized carbon/polyoxocarbosilane composites [84]. In the liquid phase, the mechanism of polyoxocarbosilane formation is certainly more complex, but the reduction by carbonaceous photoproducts is supported by detection of tiny amounts of iron carbide in the topmost layers of etched silica surface.

Both paths (Scheme 1) allow initial formation of a-Fe/Fe_2O_3/(Si/C/O)/polymer/carbon nanosols that undergo aging process resulting in the sedimentation of the nanocomposite a-Fe/Fe_2O_3/(Si/C/O)/polymer/carbon particles. Exposure of the nanocomposites to air and heating leads to oxidative depletion of Fe nanophase (a growth of the crystalline α-Fe_2O_3 nanophase).

4. Conclusions

The UV photolysis of Fe(II) acetylacetonate was accomplished for the first time by intense KrF laser irradiation of the chelate in 2-propanol. The reaction is dominated by extrusion of zero-valent iron and formation of poly(oxocarbosilane) through etching of reactor quartz by organic photoproducts.

The photolysis allows initial formation of colloids that undergo aging process to ultrafine sediment composed of Fe, C, Si and O elements and characterized as Fe/((Si/C/O)/polymer)/carbon nanocomposite. This nanocomposite contains rather rare [85–87] amorphous iron phase.

The nanocomposite is heterogeneous with respect to Fe concentration and undergoes ambient temperature oxidation of superficial Fe layer to create a discontinuous a-Fe_2O_3 passivation shell.

Further oxidation of the nanocomposite at 500 °C leads to formation of Fe_2O_3 nanobodies solely in crystalline α-phase.

Detailed analysis of magnetic properties of the nanocomposite reveals superantiferromagnetic behaviour which is ascribed to nanosized structure of the amorphous Fe_2O_3 passivating shell.

The described photolysis represents a clean and simple one-step approach to a-Fe/(Si/C/O)/carbon colloids and nanocomposite that belong, due to their interesting magnetic properties, to family of promising nanomagnetic materials.

Acknowledgements

The authors thank GA ASCR (Grant No. 400720619) for financial support and Dr. J. Boháček for TEM analyses.

References

[1] T. Klapcinski, A. Galeski, M. Kruszewski, J. Appl. Polym. Sci. 58 (1995) 1007–1013.
[2] A. Petri-Fink, M. Chastellain, L. Juillerat-Jeanneret, A. Ferrari, H. Hofmann, Biomaterials 26 (2005) 2685–2694.
[3] X.-D. Tong, B. Xue, Y. Sun, Biotechnol. Prog. 17 (2001) 134–139.
[4] S.R. Rudge, T.L. Kurtz, C.R. Vessely, L.G. Catterall, D.L. Williamson, Biomaterials 21 (2000) 1411–1420.
[5] Z. Ma, Y. Guan, H. Liu, J. Magn. Magn. Mater. 301 (2006) 469–477.
[6] R. Tongpool, S. Jindasuwan, Sens. Actuators B 106 (2005) 523–528.
[7] A. Tomescu, R. Alexandrescu, I. Morjan, F. Dumitrache, L. Florescu, R. Birjega, I. Soare, G. Prodan, Z. Bastl, A. Galikova, J. Pola, J. Mater. Sci. 42 (2007) 1838–1846.
[8] F. Li, C. Vipulanandan, K.K. Mohanty, Colloids Surf. A 223 (2003) 103–112.
[9] W.X. Zhang, J. Nanopart. Res. 5 (2003) 323–332.
[10] K. Suslick, T. Hyeon, M. Fang, Chem. Mater. 8 (1996) 2172–2179.
[11] D. Farrell, S.S. Majetich, J.P. Wilcoxon, J. Phys. Chem. B 107 (2003) 11022–11030.
[12] D.L. Huber, E.L. Venturini, J.E. Martin, P.P. Provencio, R.J. Patel, J. Magn. Magn. Mater. 278 (2004) 311–316.
[13] T. Majima, T. Ishii, Y. Matsumoto, M. Takami, J. Am. Chem. Soc. 111 (1989) 2417–2422.
[14] J.H. Yu, D.W. Lee, B.K. Kim, T. Jang, J. Magn. Magn. Mater. 304 (2006) e16–e18.
[15] C. Yang, J. Xing, Y. Guan, J. Liu, H. Liu, J. Alloys Compd. 385 (2004) 283–287.
[16] K.C. Huang, S.H. Ehrman, Langmuir 23 (2007) 1419–1426.
[17] A. Alqudami, S. Annapoorni, S. Lamba, P.C. Kothari, R.K. Kotnala, J. Nanosci. Nanotechnol. 7 (2007) 1993–2903.
[18] Y.S. Kang, S. Risbud, J.F. Rabolt, P. Stroeve, Chem. Mater. 8 (1996) 2209–2211.
[19] L. Vayssières, C. Chanéac, E. Tronc, J.P. Jolivet, J. Colloid. Interface Sci. 205 (1998) 205–212.
[20] R. Vijayakumar, Yu. Koltypin, I. Felner, A. Gedanken, Mater. Sci. Eng. A 286 (2000) 101–105.
[21] H. Ilida, K. Takayanagi, T. Nakanishi, T. Osaka, J. Colloid. Interface Sci. 314 (2007) 274–280.
[22] T. Hyeon, S.S. Lee, J. Park, Y. Chung, H.B. Na, J. Am. Chem. Soc. 123 (2001) 12798–12801.
[23] S. Sun, H. Zeng, J. Am. Chem. Soc. 124 (2002) 8204–8205.
[24] J. Rockenberger, E.C. Scher, P. Alivisatos, J. Am. Chem. Soc. 121 (1999) 11595–11596.
[25] T. Fried, G. Shemer, G. Markovich, Adv. Mater. 13 (2001) 1158–1161.
[26] M. Mikhaylova, D.K. Kim, N. Bobrysheva, M. Osmolowsky, V. Semenov, T. Tsakalakos, M. Muhammed, Langmuir 20 (2004) 2472–2477.
[27] S. Si, C. Li, X. Wang, D. Yu, Q. Peng, Y. Li, Cryst. Growth Des. 5 (2005) 391–393.
[28] D. de Caro, T.O. Ely, A. Mari, B. Chaudret, E. Snoeck, M. Respaud, J.M. Broto, A. Fert, Chem. Mater. 8 (1996) 1987–1991.
[29] D. Mahajan, A. Desai, M. Rafailovich, M.-H. Cui, N.-L. Yang, Compos. B: Eng. 37 (2006) 74–80.
[30] H. Pu, F. Jiang, Z. Yang, Mater. Lett. 60 (2006) 94–97.
[31] J. Huo, H. Song, X. Chen, S. Zhao, C. Xu, Mater. Chem. Phys. 101 (2007) 221–227.
[32] P.-Z. Si, Z.-D. Zhang, D.-Y. Geng, C.-Y. You, X.-G. Zhao, W.-S. Zhang, Carbon 41 (2003) 247–251.
[33] S. Tomita, M. Hikita, M. Fujii, S. hayashi, K. Yamamoto, Chem. Phys. Lett. 316 (2000) 361–364.

[34] F. Dumitrache, I. Morjan, R. Alexandrescu, R.E. Morjan, I. Voicu, I. sandu, I. Soare, M. Ploscaru, C. Fleaca, V. Ciupina, G. Prodan, B. Rand, R. Brydson, A. Woodword, Diamond Relat. Mater. 13 (2004) 362–370.
[35] B.H. Sohn, R.E. Cohen, Chem. Mater. 9 (1997) 264–269.
[36] C.R. Mayer, V. Cabuil, T. Lalot, R. Thouvenot, Angew. Chem., Int. Ed. 38 (1999) 3672–3675.
[37] R.V. Kumar, Yu. Koltypin, Y.S. Cohen, Y. Cohen, D. Aurbach, O. Palchik, I. Felner, A. Gedanken, J. Mater. Chem. 10 (2000) 1125–1129.
[38] H. Okada, K. Sakata, T. Kunitake, Chem. Mater. 2 (1990) 89–91.
[39] E. Kroll, F.M. Winnik, Chem. Mater. 8 (1996) 1594–1596.
[40] P.A. Dresco, V.S. Zaitsev, R.J. Gambino, B. Chu, Langmuir 15 (1999) 1945–1951.
[41] J. Pola, Z. Bastl, V. Vorlíček, F. Dumitrache, R. Alexandrescu, I. Morjan, I. Sandu, V. Ciupina, Appl. Organometal. Chem. 18 (2004) 337–342, and references therein.
[42] M. Fröba, R. Köhn, G. Bouffaud, O. Richard, G. Van Tendeloo, Chem. Mater. 11 (1999) 2858–2865.
[43] M. Iwamoto, T. Abe, Y. Tachibana, J. Mol. Catal. A: Chem. 155 (2000) 143–153.
[44] N.F. Borelli, D.L. Morse, J.W.H. Schreurs, J. Appl. Phys. 54 (1983) 344–3350.
[45] K.C. Barick, B.S.D.Ch.S. Vasaprasad, B.P. Singh, D. Bahadur, J. Non-Cryst. Solids 351 (2005) 3693–3698.
[46] S. Solinas, G. Piccaluga, M.P. Morales, C.J. Serna, Acta Mater. 49 (2001) 2805–2811.
[47] C. Slavii, M. Popovici, C. Enache, J. Šubrt, D. Niznansky, S. Bakardjieva, C. Caizer, I. Hrianca, Solid State Ionics 151 (2002) 219–227.
[48] J. Xu, S. Thompson, E. O'Keefe, C.C. Perry, Mater. Lett. 58 (2004) 1696–1700.
[49] I.K. Battisha, H.H. Afify, I.M. Hamada, J. Magn. Magn. Mater. 292 (2005) 440–446.
[50] K. Woo, J. Hong, J.-P. Ahn, J. Magn. Magn. Mater. 293 (2005) 177–181.
[51] I.K. Battisha, H.H. Afify, M. Ibrahim, J. Magn. Magn. Mater. 306 (2006) 211–217.
[52] D. Ortega, J.S. Garitaonandia, C. Barrera-Solano, M. Ramírez-del-Solar, E. Blanco, M. Domínguez, J. Non-Cryst. Solids 352 (2006) 2801–2810.
[53] X. Zhang, H. Guo, N. Chi, S.C. Wang, N.-L. Yang, D.L. Akins, Mater. Chem. Phys. 98 (2006) 207–211.
[54] R.D. Shull, L.H. Bennett, Nanostruct. Mater. 1 (1992) 83–88.
[55] J. Pola, J.P. Parsons, R. Taylor, J. Mater. Chem. 2 (1992) 1289–1292.
[56] A. Ouchi, K. Yamamoto, Y. Koga, J. Pola, J. Mater. Chem. 9 (1999) 563–566.
[57] A. Ouchi, T. Tsunoda, Z. Bastl, M. Maryško, V. Vorlíček, J. Boháček, K. Vacek, J. Pola, J. Photochem. Photobiol. A: Chem. 171 (2005) 255–256.
[58] A. Ouchi, Z. Bastl, J. Boháček, J. Šubrt, J. Pola, Surf. Sci. Technol. 201 (2007) 4728–4733.
[59] J. Pola, A. Ouchi, S. Bakardjieva, M. Urbanová, J. Boháček, J. Šubrt, J. Photochem. Photobiol. A: Chem. 192 (2007) 84–92.
[60] J.H. Scofield, J. Electron Spectrosc. Relat. Phenom. 8 (1976) 129.
[61] NIST Electron Inelastic-Mean-Free-Paths Database Version 1.1, NIST Gaithersburg, MD 20899, USA 2000.
[62] R.L. Lintvedt, in: A.W. Adamson, P.D. Fleischauer (Eds.), Concepts of Inorganic Photochemistry, Wiley, New York, 1975, p. 299 (Chapter 7).
[63] JCPDS PDF-2 Release 2001, ICDD Newton Square, PA, USA.
[64] http://srdata.nist.gov/xps/index.htm.
[65] J. Pola, A. Galíková, A. Galík, V. Blechta, Z. Bastl, J. Šubrt, A. Ouchi, Mater. Chem. 14 (2002) 144–153, and references therein.
[66] J. Pola, A. Ouchi, K. Vacek, A. Galíková, V. Blechta, J. Boháček, Solid State Sci. 5 (2003) 1079–1086.
[67] R.G.J. Miller, H.A. Willis (Eds.), Infrared Structural Correlation Tables and Data Cards, Heyden & Son, Spectrum House, London, 1969, Table 9.
[68] B. Velde, R. Couty, J. Non-Cryst. Solids 94 (1987) 238–250.
[69] C.F. Bohren, D.R. Huffman, Absorption and Scattering of Light by Small Particles, Wiley, New York, 1983.
[70] Y.-S. Shon, S.M. Gross, B. Dawson, M. Porter, R.W. Murray, Langmuir 16 (2000) 6555–6561.
[71] Y. Takeda, C.G. Lee, N. Kishimoto, Nucl. Instrum. Methods Phys. Res. B 190 (2002) 797–801.
[72] P. Fabriziolli, T. Bürgi, M. Burgener, S. van Doorslaer, A. Baiker, J. Mater. Chem. 23 (2002) 619–630.
[73] S. Morup, D.E. Madsen, C. Frandsen, C.R.H. Bahl, M. Hansen, J. Phys.: Condens. Matter. 19 (2007) 1–31.
[74] J. Cohen, K.M. Creer, R. Pauthenet, K. Srivastava, J. Phys. Soc. Jpn. 17 (Suppl. B-I) (1962) 685–689.
[75] B. Wei, M. Shima, R. Pati, S.K. Nayak, J. Singh, R. Ma, Y. Li, Y. Bando, S. Nasu, P.M. Ajayan, Small 2 (2006) 804–809.
[76] H. Tokoro, S. Fujii, T. Oku, J. Magn. Magn. Mater. 290–291 (2005) 141–144.
[77] X. Cao, R. Prozorov, Yu. Koltypin, G. Kataby, I. Felner, A. Gedanken, J. Mater. Res. 12 (1997) 402–406.
[78] D.L.A. de Faria, S. Venancio Silva, M.T. De Oliveira, J. Raman Spectrosc. 28 (1997) 873–878.
[79] I. Chamritski, G. Burns, J. Phys. Chem. B (2005) 4965–4968.
[80] J.H. Dias da Silva, S.W. Da Silva, J.C. Galzerani, J. Appl. Phys. 77 (1995) 4044–4048.
[81] J. Wang, H. Niino, A. Yabe, Appl. Phys. A 68 (1999) 111–113.
[82] H. Niino, Y. Kawaguchi, T. Sato, A. Narazaki, T. Gumpenberger, R. Kurosaki, Appl. Surf. Sci. 252 (2006) 4387–4391.
[83] R. Böhme, S. Pissadakis, D. Ruthe, K. Zimmer, Appl. Phys. A 85 (2006) 75–78.
[84] J. Pola, S. Bakardjieva, M. Maryško, V. Vorlíček, J. Šubrt, Z. Bastl, A. Galíková, A. Ouchi, J. Phys. Chem. C 111 (2007) 16818–16826.
[85] K.S. Suslick, S.-B. Choe, A.A. Cichowlas, M.W. Grinstaff, Nature 353 (1991) 414–416.
[86] G. Kataby, Yu. Koltypin, A. Ulman, I. Felner, A. Gedanken, Appl. Surf. Sci. 201 (2002) 191–195.
[87] G. Shen, M.L. Rivers, S.R. Sutton, N. Sata, V.B. Prakapenka, J. Oxley, K.S. Suslick, Phys. Earth Planet. Inter. 143–144 (2004) 481–495.